Author/s:
Farrington, RJ;Moresi, LN;Capitanio, FA

Title:
The role of viscoelasticity in subducting plates

Date:
2014-11-01

Citation:
Farrington, R. J., Moresi, L. N. & Capitanio, F. A. (2014). The role of viscoelasticity in subducting plates. Geochemistry Geophysics Geosystems, 15 (11), pp.4291-4304. https://doi.org/10.1002/2014GC005507.

Persistent Link:
https://hdl.handle.net/11343/52681

AGU PUBLICATIONS

Geochemistry, Geophysics, Geosystems

RESEARCH ARTICLE

10.1002/2014GC005507

Key Points:
- We study the effect of viscoelastic stresses on numerical subduction models
- Hinge energy rates and apparent viscosity are quantified
- Elastic slabs are less dissipative, energy is transferred within hinge region

Correspondence to:
R. J. Farrington
rebecca.farrington@monash.edu

Citation:
Farrington, R. J., L.-N. Moresi, and F. A. Capitanio (2014), The role of viscoelasticity in subducting plates, *Geochem. Geophys. Geosyst.*, *15*, 4291–4304, doi:10.1002/2014GC005507.

Received 17 JUL 2014
Accepted 17 OCT 2014
Accepted article online 25 OCT 2014
Published online 24 NOV 2014

The role of viscoelasticity in subducting plates

R. J. Farrington[1], L.-N. Moresi[2], and F. A. Capitanio[1]

[1]School of Earth, Atmosphere and Environment, Monash University, Clayton, Victoria, Australia, [2]School of Earth Sciences, University of Melbourne, Melbourne, Victoria, Australia

Abstract Subduction of tectonic plates into Earth's mantle occurs when one plate bends beneath another at convergent plate boundaries. The characteristic time of deformation at these convergent boundaries approximates the Maxwell relaxation time for olivine at lithospheric temperatures and pressures, it is therefore by definition a viscoelastic process. While this is widely acknowledged, the large-scale features of subduction can, and have been, successfully reproduced assuming the plate deforms by a viscous mechanism alone. However, the energy rates and stress profile within convergent margins are influenced by viscoelastic deformation. In this study, viscoelastic stresses have been systematically introduced into numerical models of free subduction, using both the viscosity and shear modulus to control the Maxwell relaxation time. The introduction of an elastic deformation mechanism into subduction models produces deviations in both the stress profile and energy rates within the subduction hinge when compared to viscous only models. These variations result in an apparent viscosity that is variable throughout the length of the plate, decreasing upon approach and increasing upon leaving the hinge. At realistic Earth parameters, we show that viscoelastic stresses have a minor effect on morphology yet are less dissipative at depth and result in an energy transfer between the energy stored during bending and the energy released during unbending. We conclude that elasticity is important during both bending and unbending within the slab hinge with the resulting stress loading and energy profile indicating that slabs maintain larger deformation rates at smaller stresses during bending and retain their strength during unbending at depth.

1. Introduction

Earth's rocks exhibit both viscous and elastic behaviors depending on the time scale of loading and observation. On a short time scale of seconds to tens of years the lithosphere and mantle behave as an elastic solid, however on a time scale of millions of years the mantle can be treated as a viscous fluid [*Watts and Zhong*, 2000]. There is no clear understanding as to which mechanism most influences subduction, a process that occurs on time scales between these end-members.

The Earth is considered to be a Maxwell viscoelastic material, with applied stresses decaying exponentially with time. A Maxwell viscoelastic material produces strain rates that are proportional to the sum of the stress and stress rate. Using this rheological model, viscoelastic deformation can be characterized by the Maxwell relaxation time, α, defined as the ratio of viscosity to shear modulus, giving the time required for the decay of stresses to $1/e$ of the original value. Elastic properties within the lithosphere and mantle are relatively well constrained with a shear modulus between 10^{10} and 10^{11} Pa. The viscosity within the lithosphere, as a function of temperature and pressure, can range from approximately mantle viscosities up to 10^5 times that value [*Karato and Wu*, 1993], with estimates from $<10^{21}$ Pa s [*Billen and Gurnis*, 2001] to 10^{25} Pa s [*Capitanio and Morra*, 2012]. This results in a relaxation time for the lithosphere of between 400 and 4×10^6 years. The uppermost region of the lithosphere deforms in a pressure-dependent brittle failure mode under applied stress that can be described by Byerlee's law [*Byerlee*, 1978]. The hot ductile lower most portion of the lithosphere produces deformation of a power law form [*Goetze and Evans*, 1979]. The mid-depth, high-strength region of the lithosphere supports large stresses under bending deformation naturally found within the hinge of a subducting plate.

The deformation mechanisms within the Earth are dependent on pressure, temperature, and stress. Laboratory experiments show a temperature-dependent nonlinear viscosity producing a highly viscous, cold upper lithosphere [*Karato and Wu*, 1993] weakening under bending [*Goetze and Evans*, 1979] with yielding occurring for stresses larger than $\approx$500 MPa [*Kohlstedt et al.*, 1995].

The lower lithosphere, with temperatures approaching those found in the mantle, has a significantly lower viscosity. During bending, lithospheric strength results from a thin layer only a few 10s of km thick, with a viscosity up to 10^{25} Pa s and strain rates as small as 10^{-15} s^{-1} [*Gerya and Yuen*, 2007; *Faccenda et al*., 2008, 2009]. This thin, strong central region is also suggested from the bending mechanics of oceanic lithosphere along subduction trenches [*Walcott*, 1970; *Turcotte et al*., 1978; *Watts et al*., 1980].

Deformation time scales for the lithosphere at subduction zones are dominated by bending at the hinge and can be approximated by the time required for material to travel at a subduction velocity (e.g., 6 cm/yr) through the hinge, e.g., through $\pi/4$ arc of radius 400 km[*Conrad and Hager*, 1999]. The upper limit on the time scale of deformation is therefore approximately 10^6 years, producing strain rates of 10^{-13} s^{-1}. Comparing this lithospheric deformation time scale to the lithospheric Maxwell relaxation time shows that subduction can take place on time scales where both viscous and elastic components are expected to play a role.

In a dynamic view, subduction occurs through the balance of driving and resistive forces with the negative buoyancy of the plate working against the resistive forces of viscous drag within the mantle and plate bending at the hinge. It has been shown that slabs sink at their stokes velocity with the horizontal components of subduction, plate velocity and trench retreat, determined through resisting forces [*Capitanio et al*., 2007; *Funiciello et al*., 2008; *Di Giuseppe et al*., 2008]. Furthermore, this horizontal motion of plates is controlled by the hinge and therefore defines the tectonic style of subduction on Earth [*Bellahsen et al*., 2005; *Stegman et al*., 2010]. Stresses within the hinge are therefore key to understanding the dynamics of subduction on Earth. The role of elasticity on the force balance produced during subduction and on the resulting horizontal motions of the lithosphere therefore warrants detailed analysis.

Viscoelasticity of the lithosphere is often present in models [*Beaumont*, 1978; *Burov and Diament*, 1992; *Watts and Zhong*, 2000]. A common approach assumes an elastic lithosphere, with topography and gravity observations of oceanic plates allowing for the estimation of plate strength from static elastic bending solutions including *Turcotte and Schubert* [1982], *McAdoo and Sandwell* [1985], and *Buiter et al*. [1998]. *Billen and Gurnis* [2005] found a reduction in the effective elastic strength within the fore bulge. However, *Craig and Copley* [2014] found that the presence of permanent deformation and observational noise restricts the accuracy of rheological estimates from elastic plate models.

Funiciello et al. [2003] implemented a viscoelastic rheology in numerical models of subduction, performing a range of numerical simulations to investigate its effect on subducting slab dynamics. Similar methodologies have addressed the details of viscoelastic stress within the bending zone during subduction, although a comparison between viscous and viscoelastic rheology was lacking [*Capitanio et al*., 2009; *Capitanio and Morra*, 2012]. *Mühlhaus and Regenauer-Lieb* [2005] and *Moresi et al*. [2002] have studied the role of elasticity in mantle convection, comparing the viscous case to that of viscoelastic, and *Kaus and Becker* [2007] discussed the effect of elasticity on layered Rayleigh-Taylor instabilities. However, a systematic study into the effects of elastic stresses on models of free subduction has yet to be completed. *Morra and Regenauer-Lieb* [2006], *Funiciello et al*. [2003], *Capitanio et al*. [2007], *Yamato et al*. [2007], and *Royden and Husson* [2006] have included a viscoelastic slab in subduction models, without explicitly studying the effects of the elastic component across a range of parameters.

In this study, we implement a viscoelastic rheology, give a comparison between the viscous and viscoelastic stresses and their resulting energetics and show implications for the evolution of subduction zones.

2. Governing Equations

The strain rate in a Maxwell viscoelastic material is given by the sum of the elastic and viscous strain rates,

$$D_{ij}=D_{ij}^{v}+D_{ij}^{e}=\frac{\tau_{ij}}{2\eta}+\frac{\dot{\tau}_{ij}}{2\mu} \tag{1}$$

where

$$\dot{\tau}_{ij}=\lim_{\delta t\to 0}\frac{\tau(t,x(t))-\tau(t-\delta t,x(t-\delta t))}{\delta t} \tag{2}$$

with D the strain rate tensor, τ the deviatoric stress, η the shear viscosity, μ the shear modulus, and t the current time step. Note that $\mu\to\infty$ gives a purely viscous deformation rate. Writing $\dot{\tau}$ as a finite difference, substitution into equation (1) and solving for τ gives

$$\tau_{ij}(t,x(t))=2\eta_{\mathrm{eff}}D_{ij}(t,x(t))+\frac{\eta_{\mathrm{eff}}}{\mu\Delta t}\overset{\vee}{\tau}(t-\Delta t,x(t)) \tag{3}$$

where $\eta_{\mathrm{eff}}=(\eta\Delta t)/(\alpha+\Delta t)$ with $\alpha=\eta/\mu$, the Maxwell relaxation time, and $\overset{\vee}{\tau}$ the stress history term advected and rotated into the current reference frame using the velocity field **u**, to be discussed in section 3. Substitution of equation (3) into the conservation of momentum equation, defined as

$$\sigma_{ij,j}=\tau_{ij,j}-p_i=f_i \tag{4}$$

where σ is the total stress tensor, p the isotropic pressure, and f_i a buoyancy force term, gives

$$(2\eta_{\mathrm{eff}}D_{ij})_{,j}-p_{,i}=f_i-\frac{\eta_{\mathrm{eff}}}{\mu\Delta t}\tau^{\vee}_{ij,j} \tag{5}$$

This implementation of viscoelasticity, after *Moresi et al*. [2003], modifies the momentum equation using an effective viscosity and an additional force term dependent on material properties, the time step size, and the stress history. Equation (5) coupled with the conservation of mass, $u_{i,i}=0$, provides the solution for a Maxwell viscoelastic material deforming under the Boussinesq approximation for infinite Prandtl, low Reynolds incompressible flow.

Plasticity can be introduced as a reduced effective viscosity, such that $\eta_{red}=min(\eta,\tau_y/2D)$, with D the second invariant of the strain rate tensor, ensuring yielding for stresses equal to or greater than τ_y, a specified yield stress [*Moresi et al*., 2003].

3. Numerical Implementation

3.1. Stress History

The inclusion of a stress history term into the momentum equation requires further attention. This viscoelastic rheology is implemented using the FEM-PIC code "Underworld" [*Moresi et al*., 2007]. The numerical implementation of the FEM-PIC integration within Underworld requires the stress history to be carried on a particle that is immersed in the fluid and is advected and rotated as required by the velocity **u**. As such, the stress history tensor must be transported into the current reference frame. This is possible by introducing a new operator $\mathcal{T}$ that ensures the stress on the transported particle, p, at location **x**, and time t is objective under advection and rotation over the interval Δt.

$$\begin{aligned}\overset{\vee}{\tau}{}^{t}_{ij}(t,\mathbf{x},\mathbf{u})&=\mathcal{T}^{x_p^t}_{\Delta t}(\tau_{ij}^{t-\Delta t}(\mathbf{x}_p^{t-\Delta t}),\mathbf{x},\mathbf{u})\\&=\pounds_1(\tau_{ij}^{t-\Delta t},\mathbf{x},\mathbf{u})+\pounds_2(\tau_{ij}^{t-\Delta t},\mathbf{x},\mathbf{u})\end{aligned} \tag{6}$$

where $\pounds_1\equiv u_k.\partial\tau_{ij}/\partial x_k$ accounts for the advection of stress on the particle through a velocity field given by u_k, and $\pounds_2=\tau_{ik}w_{kj}+\tau_{jk}w_{ki}$ is the Jaumann stress rate and accounts for rotation [*Eringen*, 1967], with w the vorticity tensor. The Jaumann term is not a constitutive parameter as it accounts for the passive rotation of material through a velocity field or the rotation of the observer. Taking a first-order integration of the rotation term, $\pounds_2$, produces values tangential to the rotation, thus providing an unconditionally unstable numerical update. Integration of the Jaumann derivative with a higher-order accurate method is required to produce stable solutions to the rotation of the stress history term through a velocity field.

It should also be noted that there are other terms which may be added to this definition accounting for other changes in reference frame including stretching by way of the Oldroyd derivative as discussed at length by *Harder* [1991]. Including these additional terms couples stress and pressure, adding a considerable complication that is not required for mathematical consistency [*Eringen*, 1967] and are not addressed further in this study.

3.2. The Elastic Time Step

A decoupling of the observation time and numerical time step is required [*Moresi et al*., 2003]. This can be achieved by introducing an elastic time step, Δt_e, that ensures the required observation time is resolved, distinct from the smaller numerical time step, Δt_c. Since $\Delta t_e>\Delta t_c$, we must store the stress history over several time steps. This can be achieved by introducing a new term, $\tilde{\mathcal{T}}$, being the stress history term defined across n numerical time steps of size Δt_c. The stress at current time t is then defined as

$$\tau_{ij}(\mathbf{x}_p^t)=2\eta_{\text{eff}}D_{ij}(\mathbf{x}_p^t)+\frac{\eta_{\text{eff}}}{\mu\Delta t_e}\tilde{\mathcal{T}}_{\Delta t_e}^{x_p^t}(\overset{\vee}{\tau}_{ij}^{t-\Delta t_e}) \quad (7)$$

Note the presence of Δt_e in both the definition of $\tilde{\mathcal{T}}$ and in the denominator of the preceding term, with η_{eff} now defined as $(\eta\Delta t_e)/(\alpha+\Delta t_e)$. Alternatively, *Moresi et al.* [2003] showed that a running average of the stress history could be used, defined as

$$T_{ij}^t(\mathbf{x}_p^t)=(1-\phi)\,\tilde{\mathcal{T}}_{\Delta t_c}^{x_p^t}(T_{ij}^{t-\Delta t_c}(\mathbf{x}_p^{t-\Delta t_c}))+\phi\tau_{ij}^t(\mathbf{x}_p^t) \quad (8)$$

where $\phi=\Delta t_c/\Delta t_e<1$, recalling here that a consistent application of the transport operator is required to ensure that the stresses are advected and rotated into the current reference frame.

3.3. Shear Test in 2-D

This implementation can be tested and illustrated using a simple shear test, consisting of a viscoelastic material undergoing simple shear at a constant rate from a time t_0 though to t_{max}. At t_{max}, the shearing velocity is taken to zero using a no-slip velocity boundary condition. The viscoelastic stresses then decay with time while the material deformation rate remains zero. The xy component of stored stress, the nonviscous portion of the total stress, defined in equation (7) as $\tau^{\text{stor}}=\frac{\eta_{\text{eff}}}{\mu\Delta t_e}\tilde{\mathcal{T}}_{\Delta t_e}^{x_p^t}(\overset{\vee}{\tau}_{ij}^{t-\Delta t_c})$ is given by

$$\tau_{xy}^{\text{stor}}=\begin{cases}\left(e^{-\frac{\mu}{\eta}t}\left(C_2\cos\left[\frac{Vt}{h}\right]-C_1\sin\left[\frac{Vt}{h}\right]\right)-C_2\right) & \text{if } t<t_{max}\\[2ex] \left(e^{-\frac{\mu}{\eta}t_{max}}\left(C_2\cos\left[\frac{Vt_{max}}{h}\right]-C_1\sin\left[\frac{Vt_{max}}{h}\right]\right)-C_2\right)e^{-\frac{\mu}{\eta}(t-t_{max})} & \text{if } t>t_{max}\end{cases} \quad (9)$$

where V is the shear velocity along the top wall boundary, h is the height of the box, $C_1=-(V^2\eta^2\mu)/(\mu^2h^2+V^2\eta^2)$, and $C_2=-(Vh\eta\mu^2)/(\mu^2h^2+V^2\eta^2)$. All parameters used for testing are dimensionless.

Figure 1a shows the resulting xy component of the deviatoric stored stress term for a 2-D viscoelastic material across a range of Δt_e. At longer Δt_e, the stored stress appears under resolved, indicating these larger elastic time step values capture dynamics that occur on time scales approximately equal to or greater than the Maxwell relaxation time, that is with a portion of viscous deformation. For shorter Δt_e, the numerically calculated stress approaches the analytic solution, indicating that the elastic time step is sufficiently small to fully capture the elastic stored stresses produced within the material under the applied strain rate.

3.4. Torsion Test in 3-D

The analytic solution outlined by equation (9) can be extended from this essentially 1-D test into 3-D by applying the shear velocity in the x-z plane. Testing of the full viscoelastic implementation including the rotation terms is possible by placing this 3-D shear test in a coordinate system under going solid body rotation. Figure 1b shows the evolution of the stress in comparison to the analytical solution of equation (9) placed within the rotating frame. The rotating frame is achieved by imposing a velocity boundary condition of a constant solid body rotation about the y axis in addition to the shearing rate. The stress within this rotating frame is given by equation (9), with the stress in the nonrotating frame found by applying a rotation matrix, R, to the nonrotating stress solution. That is, $\tau=R^{-1}\tau'R$, where $'$ denotes the rotated frame, R is the rotation matrix about the y axis given by $R=[(cos\theta,0,sin\theta),(0,1,0),(-sin\theta,0,cos\theta)]$, with $\theta=\omega t$, ω being the dimensionless rotation rate. The stress components shown in Figure 1b from within the nonrotating frame can then be given by $\tau_{xy}^{\text{stor}}=\tau_{xy}^{\text{stor}'}cos\theta$ and $\tau_{yz}^{\text{stor}}=-\tau_{xy}^{\text{stor}'}sin\theta$. It can be seen that, using a higher-order Jaumann stress rate advection scheme results in accurate stress advection and rotation within the full 3-D space plus time domain. It should be noted here that the velocity field used in this test was chosen to rigorously test the rotational terms in equation (6). Whether these rotational terms are required for individual models is dependent upon the model setup. For subducting slabs at a constant curvature, the individual parcels of material experience purely rotational effects, accounting for this within the stress history term would then be required for consistency.

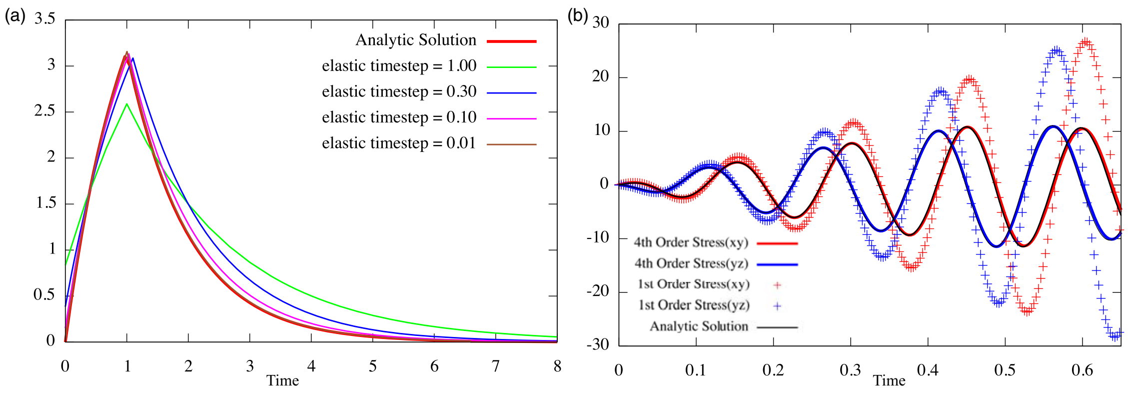

Figure 1. (a) The xy component of dimensionless stored stress with dimensionless time for the 2-D viscoelastic material undergoing simple shear and relaxation. Nondimensional material parameters of $\eta=10^2$, $\mu=10^2$, $\alpha=1$, $V=0.05$, $h=1$ with Δt_e ranging from 1 to 0.01, $t_{max}=1$, and $\Delta t_c=\Delta t_e/3$. The analytic solution outlined in equation (9) is shown in red. (b) The xy and yz stress components of a material undergoing simple shear within a 3-D rotating reference frame. Nondimensional material parameters of $\eta=10^2$, $\mu=10^2$, $\alpha=1$, $V=0.3$, $h=1$, $t_{max}=0.5$, and $\omega=42$. Note the coordinate system for this test has the *y* axis in the vertical with the *z* axis in plane. Results for a first (crosses) and fourth- (lines) order accurate Jaumann stress rate integration scheme are shown in comparison to the analytical solution (black) given by equation (9) within the rotating frame.

3.5. Analysis Parameters

The energy dissipation, E_{diss}, is a measure of the rate of change of work done within a body. The dissipation due to internal deformation is defined by $\dot{W}=\int_V \sigma_{ij} D_{ij} dV$, where σ is the shear stress, taken to be the second invariant of the deviatoric stress and D is the strain rate [*Ranalli*, 1995]. Energy in a viscous material is therefore dissipated with time per unit volume by

$$\dot{E}_{diss}=\tau_{ij}D_{ij}=2\eta_{ij}D_{ij}^2 \tag{10}$$

For a viscoelastic material, the energy rate is partitioned between dissipative (viscous) and restoring (elastic) rates with the elastic portion stored for dissipation at a later time and location. Dissipation within a viscoelastic material is calculated using only the viscous component of the strain rate, that is $\dot{E}_{diss}=\tau_{ij}D^v_{ij}$ with, from equation (1), $D^v_{ij}=D_{ij}-D^e_{ij}$. The implementation outlined in equation (3) gives

$$\dot{E}_{diss}=\tau_{ij}D^v_{ij}=\tau_{ij}[D_{ij}+\frac{\overset{\vee}{\tau}_{ij}}{2\mu\Delta t}]\frac{\eta_{\rm eff}}{\eta} \tag{11}$$

giving an elastic storage rate of

$$\dot{E}_{stor}=\tau_{ij}D^e_{ij}=\tau_{ij}(D_{ij}-D^v_{ij}) \tag{12}$$

Viscous materials are coaxial with parallel stress and strain rate eigenvectors while viscoelastic stresses are generally not coaxial with strain rate. For a viscoelastic material, an apparent viscosity can be defined, the ratio between the stress and strain rate invariants, $\eta_{app}=\tau/2\dot{\epsilon}$. For a viscoelastic material approaching purely viscous deformation, the apparent viscosity will approximate the true viscosity. However, the apparent viscosity will deviate from this true viscosity for increasingly elastic deformation. The apparent viscosity is therefore a useful parameter to illustrate the presence, or absence, of elastic stresses and its effect on the deforming material.

4. Model Setup

Here we model subduction using a single slab within an initially stationary, passive mantle. Free subduction models are preferred at this stage as they isolate the dominate forces of subduction without the added complexities of neighboring plates, lithospheric and mantle inhomogeneities, and other far field forces. In this study, a layered viscosity structure for the lithosphere is used [*Capitanio et al.*, 2007; *OzBench et al.*, 2008; *Capitanio et al.*, 2009] with three layers each with a constant viscosity, shear modulus, and cohesion representing the brittle upper lithosphere, the strong central stress guiding core, and the creeping lower lithosphere.

A slab of length 3667 km is placed along the top wall beginning 1667 km from the left side wall. The slab has a thickness of 100 km including the upper and lower viscoplastic layers of thickness 25 km.

Table 1. Parameters and Model Scalings Held Constant for All Experiments

Quantity	Symbol	Scaled Value
Domain height	H_{box}	600 km
Domain width	L_{box}	4000 km
Core height	h_{core}	50 km
Plate height	h_{plate}	100 km
Plate length	L_{plate}	3667 km
Gravitational acceleration	g	10 ms^{-2}
Plate density contrast	$\Delta\rho$	80 kg m^{-3}
Reference viscosity	η_{um}	1.4×10^{19}Pas
Viscosity of viscoplastic layers	$\Delta\eta_{vp}$	200
Yield Stress	τ_y	48 MPa

The remaining 50 km central region is modeled using either a viscous or visco-elastic material. The slab has a density contrast of 80 kg m^{-3} to that of the surrounding mantle, with the exception of the models included in Figure 6 which have density contrasts as stated. In all models, the viscosity of the upper mantle is $\eta_{um}=1.4\times10^{19}$ Pa s. The upper and lower plate layers have a viscoplastic rheology implemented using a Von Mises yield criterion, reducing the initial viscosity of $200\eta_{um}$ for a maximum stress of 48 MPa. Material parameters and model scalings are detailed in Table 1.

Subduction is initiated with a perturbation of length 100 km at an angle of 30° into the mantle, as shown in Figures 2a and 2b. After the slab tip reaches the bottom boundary, Figure 2c, subduction evolves toward a steady state with fully developed subduction and the slab supported by the mantle boundary at 600 km, Figure 2d. Measurements in this study are taken at this steady state, when subduction has consumed $\approx$1000 km of the initial plate length.

At a distance from the slab edge within Figure 2, the 3-D subducting plate is equivalent to a 2-D model as can be see by the velocity vectors and the uniform strain rate across the length of the hinge shown in Figure 2e, with the strain rate tensor containing non zero components only within the x-y plane. On this basis, 2-D models were considered in the remainder of this study. A Cartesian box with domain dimensions 4000 km $\times$ 600 km, periodic side wall, free-slip top and no-slip bottom wall velocity boundary conditions was used throughout this study.

Resolution tests show a consistent steady state slab morphology was achieved for element resolutions greater than 144 $\times$ 48; however, resolutions of at least 256 $\times$ 64 are required to constrain maximum stresses within the slab core at the hinge. A resolution of 574 $\times$ 128 (7 km $\times$ 5 km) is used for all models presented in this study.

5. Results

5.1. Role of Viscosity

The shear modulus for Earth's lithosphere is well constrained at approximately 80 GPa. In contrast, estimates of Earth's lithospheric viscosity range many orders of magnitude. A series of models were produced exploring this range with Figure 3 showing results from five subduction models with an Earth-like elastic parameter of $\mu=8\times10^{10}$Pa and increasing viscosity ranging from $\Delta\eta_{core}=6\times10^{2}$ to 6×10^{4}, Table 2 Exp. 1 to 5. Figure 3a shows the slab deflection against the slab length taking the initiation of bending at the hinge as $x=0$km. Within the hinge, the slab initially bends as it subducts into the upper mantle. The slab then unbends at depth, straightening within the mantle. The initiation of bending also marks the location of the maximum deviatoric stress, strain rate, and energy dissipation as shown in Figures 3b–3d. The bending and unbending regions can be seen within the stored energy rate shown in Figure 3e, with a positive rate indicating the storing (loading) of energy within the slab during bending and a negative rate indicating the release (unloading) of energy within the slab during unbending.

For increasing slab viscosity, Figure 3 shows a shallowing of the slab dip with a corresponding increase in stress and decrease in strain rate within the subduction hinge. The energy dissipated within the hinge remains constant while the stored energy rate magnitude increases with viscosity contrast.

Results for the apparent viscosity, shown in Figure 3f, highlight the differing dynamics between viscous and elastic stresses within the slab. The results for viscous and viscoelastic cases diverge for $\Delta\eta \geq 10^4, \alpha \geq 50\times10^3$years. For the lower Maxwell relaxation time models (blue, red), a linear relationship between the stress and strain rate can be seen throughout the slab length. For increasing relaxation times (yellow, magenta), we observe a smaller apparent viscosity leading into the slab hinge, followed by an

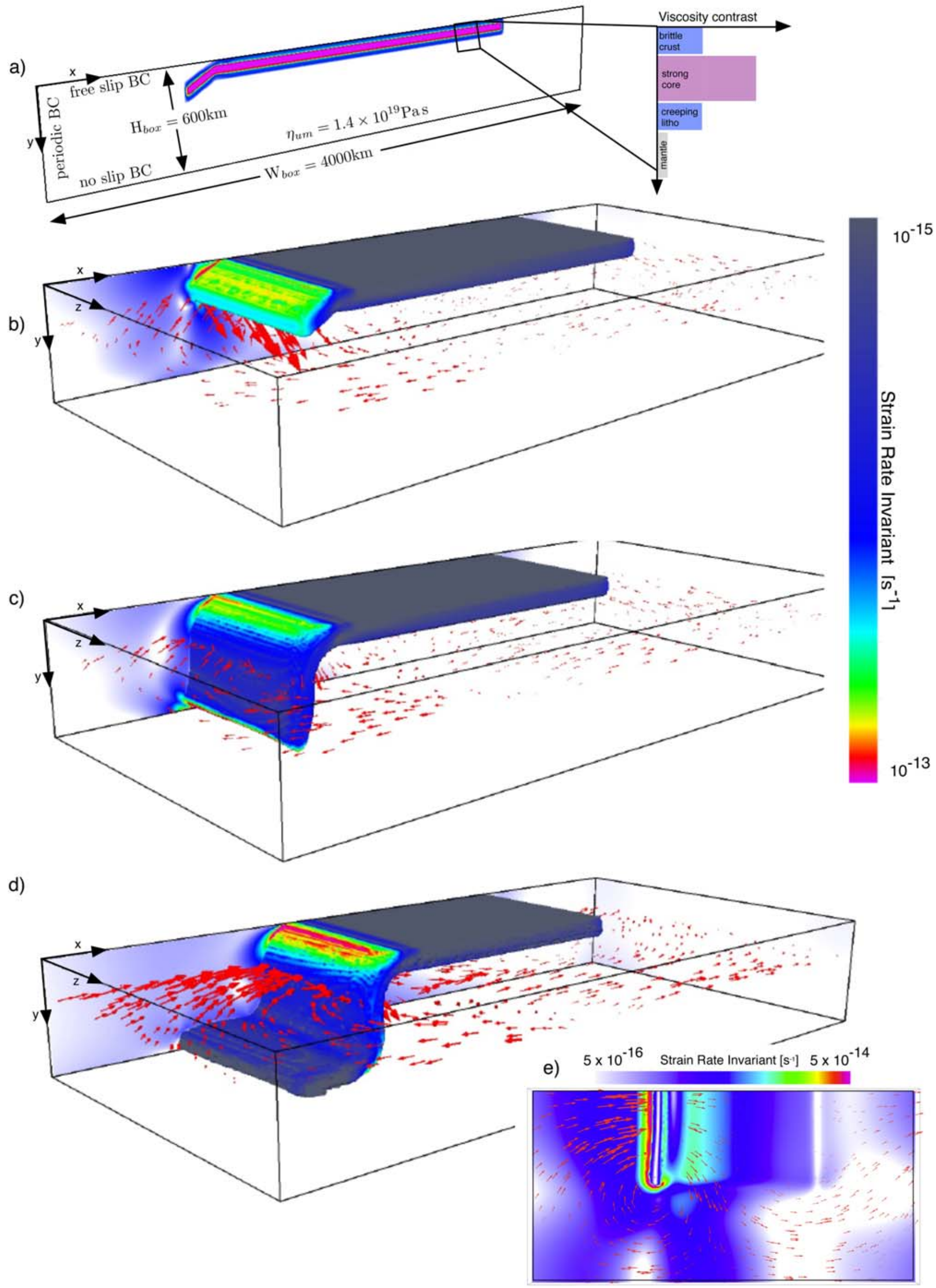

Figure 2. A viscoelastic slab model with $\Delta\eta=2\times10^3$, $\mu=8\times10^{10}$Pa, and a width of 1000 km with periodic velocity wall boundary conditions in x and mirrored in z. (a) Viscosity profile within the slab taken along the mid plane of the domain, highlighting the layered viscosity structure comprising a strong core with a surrounding, weaker lithosphere. Velocity boundary conditions, domain dimensions, and upper mantle viscosity as shown. (b) The slabs initial condition, with a perturbation of 30° as shown with a model domain of 4000 km $\times$ 600 km $\times$ 2000 km with numerical grid resolution of 288 $\times$ 64 $\times$ 144. The strain rate invariant is shown on the slab surface highlighting the location of the hinge and plotted along the bounding walls located at z = 0 km and x = 4000 km. Velocity vectors are shown at a depth of 120 km. (c) Slab tip reaching the 600 km mantle boundary. (d) Slab during steady retreating subduction. (e) Top down view of a cross section taken at 200 km depth showing the strain rate invariant and velocity vectors during steady retreating subduction.

increase in apparent viscosity leading out of the hinge. This indicates a departure from purely viscous deformation within the hinge and the transfer of elastic energy from the initial loading of the slab at the surface during bending to its release at depth during unbending.

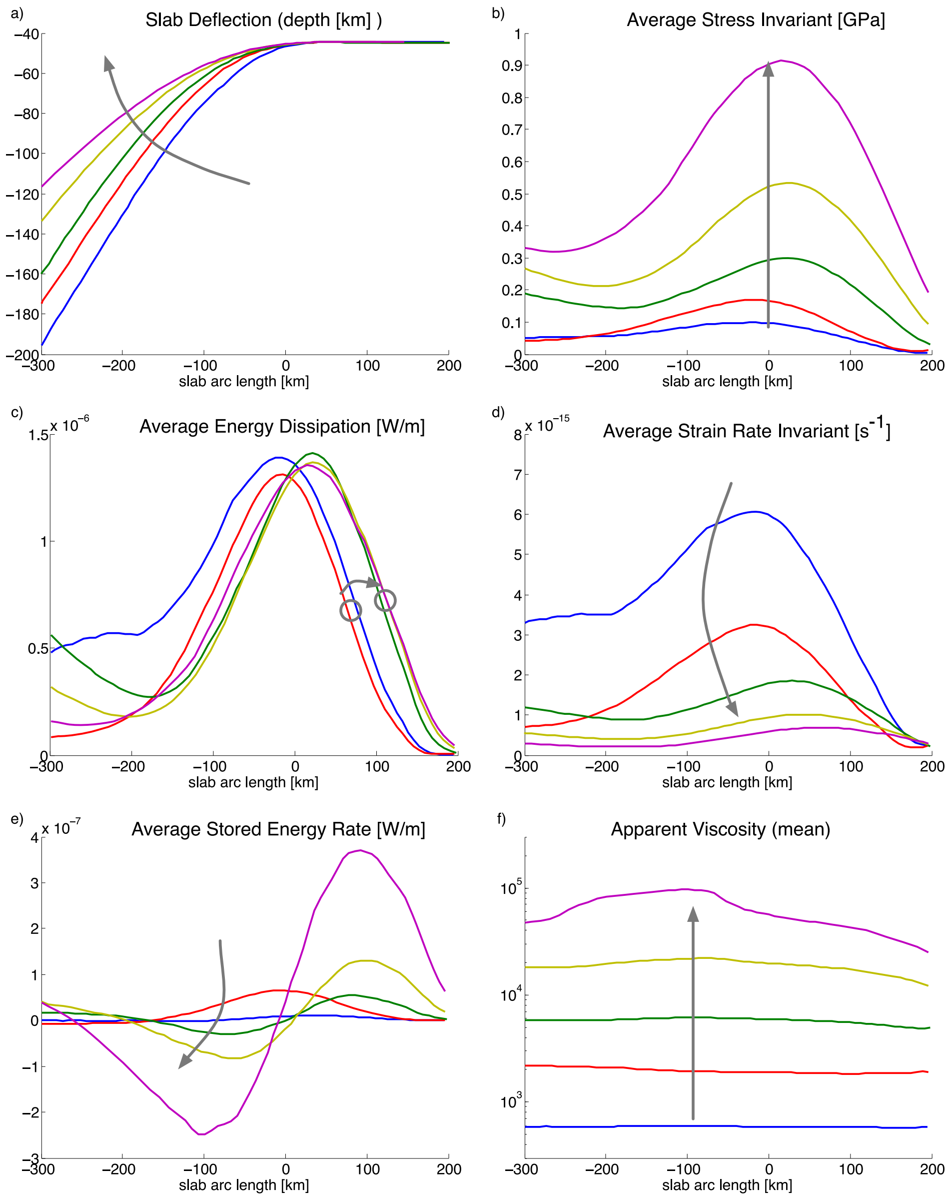

Figure 3. Results from viscoelastic slab subduction models with a shear modulus, μ, of 8×10^{10}Pa and $\Delta t_e=20\times10^3$years, for a range of core viscosity values. blue: $\Delta\eta_{core}=6\times10^2$, $\alpha=3\times10^3$years, red: $\Delta\eta_{core}=2\times10^3$, $\alpha=10\times10^3$years, green: $\Delta\eta_{core}=6\times10^3$, $\alpha=30\times10^3$years, yellow: $\Delta\eta_{core}=2\times10^4$, $\alpha=100\times10^3$years, and magenta: $\Delta\eta_{core}=6\times10^4$, $\alpha=300\times10^3$years. Figures for (a) deflection, (b) stress invariant, (c) energy dissipation, (d) strain rate invariant, (e) stored energy rate and (f) apparent viscosity within the core against slab length with 0 km taken as the initiation of bending. Gray arrows highlight the large-scale trends for increasing viscosity contrast and relaxation time.

5.2. Role of Shear Modulus

In contrast to the previous model suite, adjusting the role of elasticity via the shear modulus and holding the viscosity constant produces a suite of subduction models that share equivalent (viscous) strength and slab dip but with different Maxwell relaxation time and resulting energetics. Six models were run with a $\Delta\eta_{core}$ of 2×10^4 for a range of shear modulus values and Maxwell relaxation times (a) $\mu=\infty$, $\alpha=0$ (viscous), (b) 4×10^{11}Pa, $\alpha=2\times10^4$years, (c) 8×10^{10}Pa, $\alpha=10^5$years, (d) 4×10^{10}Pa, $\alpha=2\times10^5$, (e) 8×10^9Pa, $\alpha=10^6$, (f) 4×10^9Pa, $\alpha=2\times10^6$years, Table 2 Exp. 6 to 11. Figure 4a shows the slab deflection during steady state subduction with each having a similar morphology. A distinct fore bulge can be seen in the slab core deflection for larger Maxwell relaxation times, which is not present, nor expected, in the shorter Maxwell relaxation time, viscous dominated models.

Table 2. Model Parameters Varied for Numerical Experiments

Exp	η_{core}/η_{um}	μ_{core} (Pa)	α (years)
1	6.0×10^2	8×10^{10}	3×10^3
2	2.0×10^3	8×10^{10}	10×10^3
3	6.0×10^3	8×10^{10}	30×10^3
4	2.0×10^4	8×10^{10}	100×10^3
5	6.0×10^4	8×10^{10}	300×10^3
6	2.0×10^4	∞	0
7	2.0×10^4	4×10^{11}	20×10^3
8	2.0×10^4	8×10^{10}	100×10^3
9	2.0×10^4	4×10^{10}	200×10^3
10	2.0×10^4	8×10^9	1000×10^3
11	2.0×10^4	4×10^9	2000×10^3

Figures 4b and 4c show the stress and strain rate invariant with slab length, highlighting that for $\alpha > 2\times10^5$years, the relationship between stress and strain rate within the slab is no longer coaxial. Figures 4d and 4e outline the deviatoric stress within the least and most elastic models, respectively, both the stress invariant and orientation is shown. Figure 4d is dominated by viscous stresses as seen by the colocation of maximum stress with the maximum deformation rate (bending rate) near the surface of the slab, leading into the hinge. With increased elasticity, Figure 4e, the maximum stress moves from the region of maximum bending rate found for viscous deformation to the region of maximum curvature (deformation/bending) as expected for elastic bending.

Figure 5 shows the energy dissipation, energy storage rate, and apparent viscosity. The energy dissipation rate is inversely proportional to the Maxwell relaxation time with dissipation rates declining significantly for relaxation times greater than 2×10^5years. Figure 5b shows stored energy rates for short Maxwell relaxation times an order of magnitude smaller than respective dissipation rates. However, stored energy rates for longer Maxwell times are of the same order as dissipation rates. Stored energy rates can be seen as positive leading into the hinge and negative leading out. It is shown here that while all models with equivalent core viscosity produce very similar morphology, as shown in Figure 4a, the resulting energetics are different.

The apparent viscosity of the viscoelastic slab models shown in Figure 5c, highlighting deviations from purely viscous deformation, can be grouped into three regimes. The first shows the quasi-viscous case with the apparent viscosity equivalent to the true viscosity. The second contains intermediate Maxwell relaxation times, 10^4 years $\geq \alpha \geq 10^6$years, with apparent averaging the true viscosity along the slab length, however, deviating by an order of magnitude, decreasing leading into and increasing leading out of the hinge. A third case can be seen for relaxation times greater than 10^6 years with a significant decrease, up to 2 orders of magnitude, throughout the slab when compared to the viscous models. During bending, a decrease in apparent viscosity indicates the occurrence of increased deformation rates at smaller stresses. This can been seen by comparing the location of maximum strain rate in Figure 4c with the stress value at the same location in Figure 4b. During unbending, an increase in apparent viscosity is measured, highlighting that the maximum stress now occurs at a distance from the maximum deformation rate. This can again be seen by comparison of Figures 4b and 4c.

6. Discussion

The results presented in this study highlight the complexity of viscoelastic deformation within models of free subduction and the implications for the stresses and energetics of such processes.

Much work has been devoted to the comparison of different styles of subduction as shown by free subduction modeling, both analog and numerical, to that seen on Earth [*Stegman et al*., 2010; *Ribe*, 2010; *Capitanio and Morra*, 2012; *Bellahsen et al*., 2005; *Heuret et al*., 2007; *Faccenna et al*., 2009]. *Stegman et al*. [2010] proposed a classification of subduction styles solely on the balance between buoyancy forces and plate stiffness, combining these parameters and interpreting the large variety of model slab morphologies seen across many studies. Others have shown that the mechanics of lithospheric bending has a strong control on subduction motions [*Wu et al*., 2008; *Faccenna et al*., 2007; *Funiciello et al*., 2008] as well as bending radii and dips [*Ribe*, 2010; *Capitanio and Morra*, 2012], with a comparison between models and global compilation of radii, dips and plate velocities shown to correlate on Earth [*Capitanio and Morra*, 2012]. Our results show that these comparisons between subduction models and Earth are warranted when comparing key observables such as dip angles, fore bulge location, slab morphology, and plate motions. Yet, inferring the rheology of the lithosphere [*Funiciello et al*., 2008; *Cizkova et al*., 2007; *Billen and Hirth*, 2007] may be biased by the choice of rheological model.

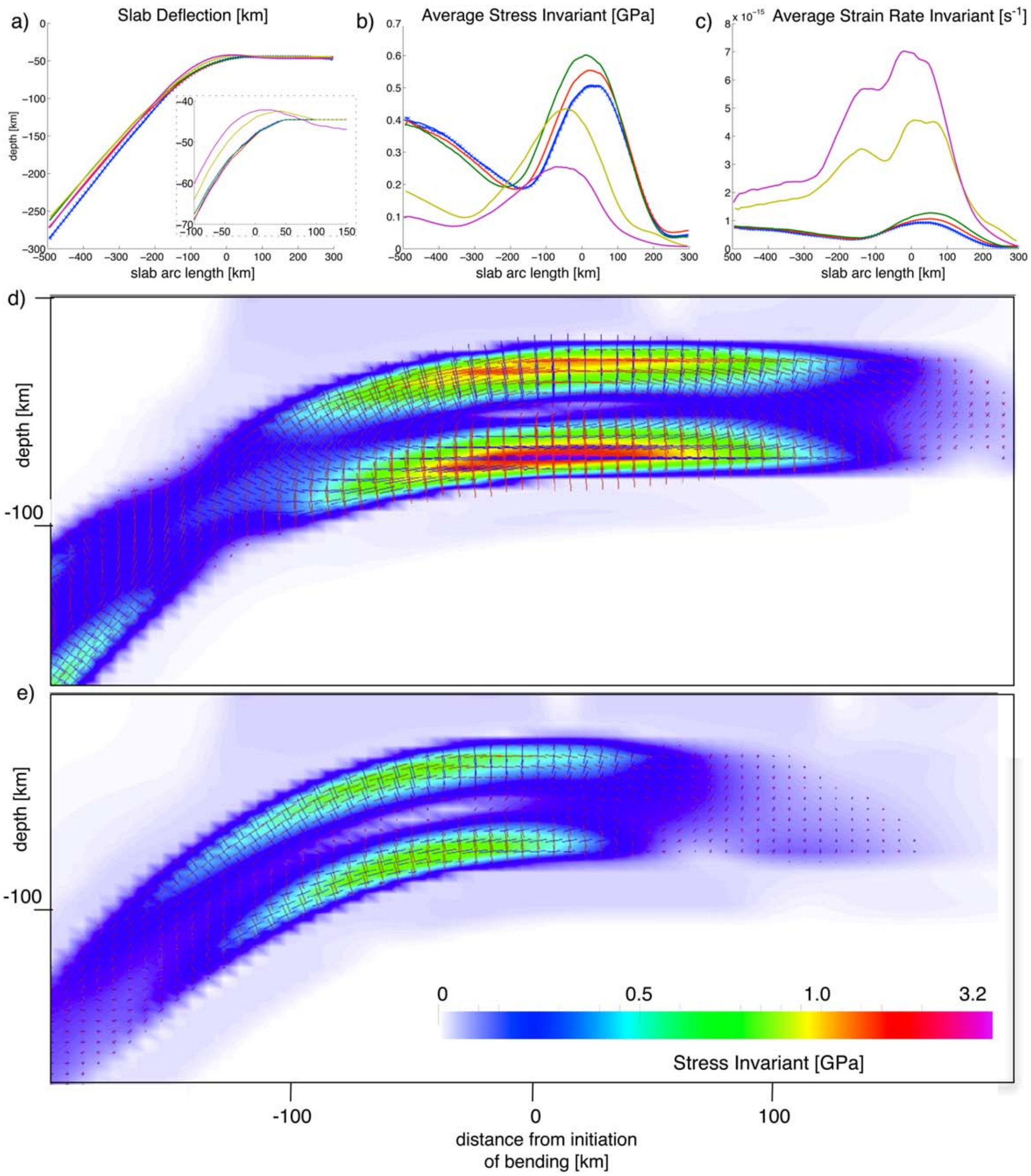

Figure 4. (a) Slab deflection, with inset highlighting the fore bulge within the hinge, (b) stress invariant, and (c) strain rate invariant within the core slab for viscoelastic subduction models with $\Delta\eta_{core}=2\times10^4$, $\Delta t_e=20\times10^3$years, for a range for shear modulus, μ values. Values are averaged within the core. Color indicates shear modulus/relaxation time with blue (dashed): $\mu=\infty$, $\alpha=0$ (viscous core), blue (solid): 4×10^{11}Pa, $\alpha=2\times10^4$years, red: 8×10^{10}Pa, $\alpha=10^5$years, green: 4×10^{10}Pa, $\alpha=2\times10^5$years, yellow: 8×10^9Pa, $\alpha=10^6$years, and magenta: 4×10^9Pa, $\alpha=2\times10^6$years. Deviatoric stress invariant (GPa) map overlaid with cross hairs of the stress eigenvectors showing extension (red) and compression (blue) for a relaxation time of (d) 2×10^4years and (e) 2×10^6years. Eigenvectors are plotted using the same scale for both Figures 4d and 4e.

In fact, as shown in Figure 4, the presence of elastic stresses has a minor effect, outside of the fore bulge, on observables such as dip angle and slab morphology, yet it does affect the apparent viscosity of the plates when bending. Estimates of viscosities averaged in the lithosphere range from 100 to 300 times the mantle viscosity [*Wu et al*., 2008; *Funiciello et al*., 2008]. Figures 3f and 5c show viscoelastic plates producing a lower apparent viscosity leading into the subduction zone when compared to viscous plate models. Thus, a larger true viscosity is required for a viscoelastic model to produce an equivalent viscosity as found in a viscous model within the shallow bending region. The Earth's lithospheric viscosity inferred by comparisons with

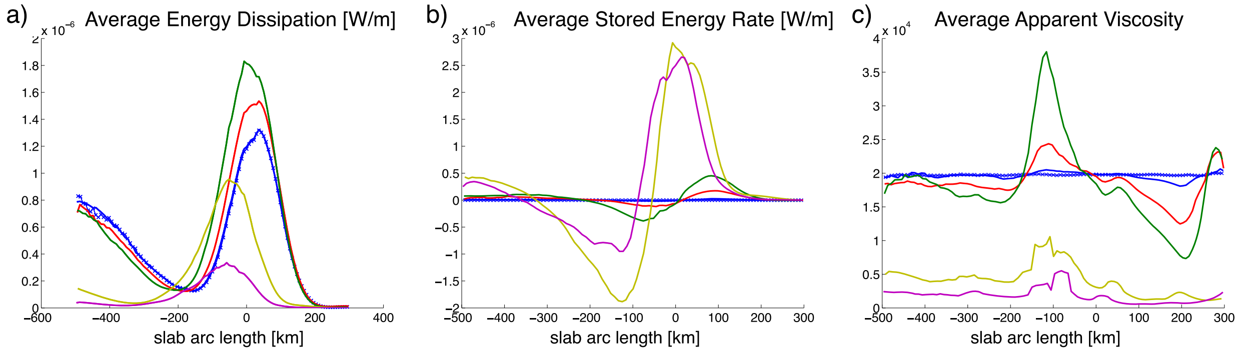

Figure 5. (a) Energy dissipation, (b) storage energy rate, and (c) apparent viscosity as shown in Figure 3. Values are averaged within the core. Color indicates shear modulus and relaxation time as for Figure 4 with blue (dashed): $\mu=\infty$, $\alpha=0$ (viscous core), blue (solid): 4×10^{11} Pa, $\alpha=2\times10^{4}$ years, red: 8×10^{10} Pa, $\alpha=10^{5}$ years, green: 4×10^{10} Pa, $\alpha=2\times10^{5}$ years, yellow: 8×10^{9} Pa, $\alpha=10^{6}$ years, and magenta: 4×10^{9} Pa, $\alpha=2\times10^{6}$ years.

viscous plates may therefore be underestimated. *Kaus and Becker* [2007] highlight this issue suggesting it may explain the low viscosity values inferred from various studies for Earth and Venus [*Billen and Houseman*, 2004; *Hoogenboom and Houseman*, 2006]. This underestimation may be compounded for averaged viscosities in slab models. *Stegman et al.* [2010] and others [*Ribe*, 2010; *Capitanio and Morra*, 2012] highlight the relationship between plate strength, thickness, and viscosity contrast, showing that strength is proportional to the cube of plate thickness. The thin core used within this study, supporting bending at the hinge, requires a viscosity contrast at least an order of magnitude greater to provide the equivalent strength of a 100 km lithosphere with an averaged viscosity to that used in laboratory models [*Schellart*, 2004; *Funiciello et al.*, 2008].

Viscosities in excess of 10^{24} Pa s are found in Earth's lithosphere [*Karato and Wu*, 1993], values 3–4 orders of magnitude larger than mantle viscosities. Similar values can be retained when lithospheres subduct at depth [*Stadler et al.*, 2010]. Models presented here, within this range of Earth-like viscosities and elasticity,

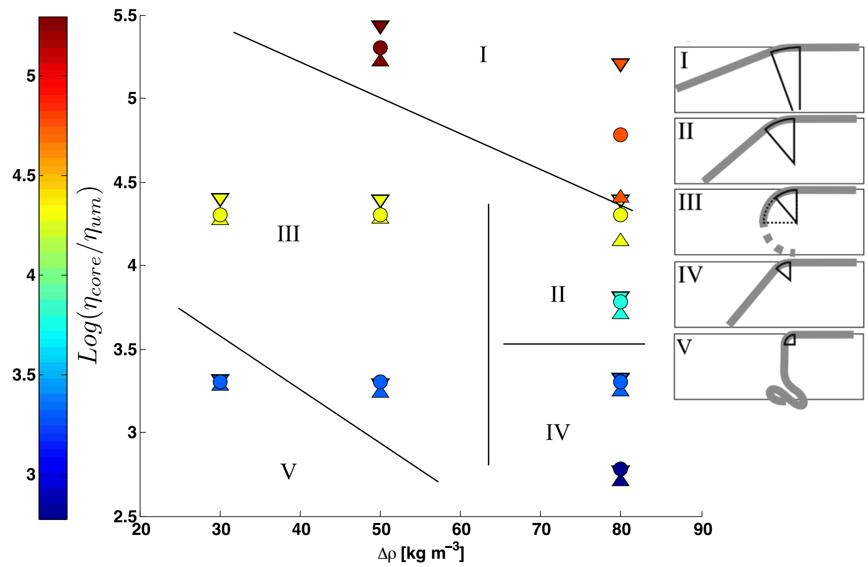

Figure 6. A subduction regime diagram showing lithospheric to upper mantle density contrast against viscosity contrast. Two sets of models are included, one with a viscoelastic rheology (triangles, with $\mu=8\times10^{10}$ Pa) and one with a viscous rheology (circles, $\mu=\infty$). The maximum and minimum apparent viscosity for the viscoelastic models are shown with downward and upward pointing triangles, respectively. The resulting steady state subduction mode is also shown with (I) flat lying strong retreat, (II) strong fold-and-retreat, (III) roll over advancing, (IV) weak retreating, and (V) weak fold-and-retreat, taken from *Capitanio and Morra* [2012], noting that the subduction mode of viscoelastic slabs does not differ from viscous slabs for equivalent viscosity and density contrast.

show a large deviation in energetics in comparison to the purely viscous solutions. In fact, this effect is maximized in the lithosphere with high-viscosity regions and larger buoyancy contrasts displaying increased elastic stresses over time. Figure 6 shows the lithospheric to upper mantle density contrast against the range of apparent viscosity contrasts within the hinge region, highlighting where Earth-like elastic stresses contribute to the energy balance during subduction with the regime diagram given in *Capitanio and Morra* [2012, Figure 9], plotting both the apparent and true viscosity within the subduction hinge. It can be seen for models with $\Delta\eta_{core} > 10^4$ and $\Delta\rho > 50$ kg m^{-3} that elastic stresses contribute to deformation within the hinge.

When scaled to Earth-like parameters, *Kaus and Becker* [2007] highlight that elastic stresses have negligible effect on the dynamic evolution of a Rayleigh-Taylor instability, yet also found stress builds up differently within the crust of viscoelastic models, as found for craton stability in *Beuchert et al*. [2010]. *Mühlhaus and Regenauer-Lieb* [2005] found that while elasticity did not have a large effect on global parameters it did have a significant effect on instabilities on the smaller scale, e.g., subduction, with *Thielmann and Kaus* [2012] finding it did not affect shear localization during subduction initiation. Thus, noting slab bending dissipation rates predicted using viscous models are unrealistically high with lower dissipation rates expected when elastic deformation is included, as shown in the results presented here.

A consequence of the inclusion of an elastic deformation mechanism is the occurrence of increased deformation rates at smaller stresses during bending. Therefore, the bending of viscous plates might not be appropriate for reproducing the Earth's lithosphere when weakening is inferred. Larger stresses in the hinge area of a viscous plate might lead to an overestimation of the weakening processes, whether viscous or plastic [*Di Giuseppe et al*., 2008; *Bellahsen et al*., 2005; *Cizkova et al*., 2007; *Stadler et al*., 2010; *Billen and Hirt*, 2007], with dissipation estimates in the bending area affected by the choice of rheology. The concentration of stress in the stiff core and the localization of deformation in the plates outer layers, resulting from bending stresses and nonlinear rheologies [*Leng and Zhong*, 2010; *Rose and Korenaga*, 2011], supports the idea that dissipation must be lower in the bending area than what is inferred from averaged viscous models. When a viscoelastic rheology is chosen, this effect is more prominent and the contribution of stored energy might reduce the dissipation to very low values, as low as 10% of the total energy dissipation found in *Capitanio et al*. [2009].

The energy balance of the system presented here reproduces the total work rate partitioning of a plate subducting into the mantle. The total energy available is simply the gravitational potential energy of the lithospheric plate. This study addresses the amount of energy dissipated within the slab during the bending of the plate, with the presence of non dissipative stresses of interest. The results presented here are therefore independent of the mechanism dissipating energy, with the total work done by these processes not likely to exceed the available energy within the slabs.

Additionally, the results discussed here have been performed in 2-D. While this is sufficient for studying the dynamics of subduction at a distance from slab edges the force balance and energetic scale found for 2-D are not guaranteed to be appropriate when considering the subduction of 3-D plate in its entirety. In *Capitanio and Morra* [2012], scaling laws were derived for curvature at hinge zones from viscoelastic 2-D models. The application to a variety of 3-D models, both analog and numerical, and observations from subduction zones on Earth suggests that the energy partitioning between mantle and lithospheres during subduction is likely to be independent of the position along the trench, although trench curvature might be different for the relevant rotation of viscous stresses around slab edges. While our models converge to the same conclusion, they suggest that viscoelasticity in three-dimensions should be more relevant in perturbed subduction zones.

7. Conclusion

The numerical implementation of a viscoelastic rheology and methodology outlined here allow for the systematic study of the introduction of elastic stresses into models of free subduction. The apparent viscosity within the subducting plate is variable throughout the length of the plate, decreasing on approach to the hinge and increasing as material exits the hinge at depth within the mantle. The results shown here highlight the differences between viscous and viscoelastic stresses at realistic Earth parameters, with viscoelastic stresses being up to an order of magnitude less dissipative at depth within the mantle resulting from the transfer of elastic energy from the bending to the unbending region within the slab. Elasticity is therefore important for stress loading during bending and the resulting energy transfer that occurs during visco-elastic subduction. The stress loading and resulting apparent viscosity produced during bending highlights that plate weakening would most likely only occur during the initial bending of the plate at the surface and is unlikely to occur at depth within the mantle, where stresses are smaller and plates keep their strength.

Acknowledgments
We thank Bruce Buffett, Boris Kaus, and an anonymous reviewer for their insightful comments. The authors acknowledge support from the Australian Research Council's Discovery Projects funding scheme (projects DP0878501, DP1095166, DE130100604) and the use of NCI National Facility in Canberra, Australia, which is supported by the Australian Commonwealth Government. Underworld development was supported by AuScope, under the National Collaborative Research Infrastructure Strategy.

References

Beaumont, C. (1978), The evolution of sedimentary basins on a viscoelastic lithosphere: Theory and examples, *Geophys. J. R. Astron. Soc.*, *55*, 471–497.
Bellahsen, N., C. Faccenna, and F. Funiciello (2005), Dynamics of subduction and plate motion in laboratory experiments: Insights into the "plate tectonics" behaviour of the earth, *J. Geophys. Res.*, *110*, B01401, doi:10.1029/2004JB002999.
Beuchert, M. J., Y. Y. Podladchikov, N. S. C. Simon, and L. H. Rüpke (2010), Modeling of craton stability using a viscoelastic rheology, *J. Geophys. Res.*, *115*, B11413, doi:10.1029/2009JB006482.
Billen, M., and M. Gurnis (2001), A low viscosity wedge in subduction zones, *Earth Planet. Sci. Lett.*, *193*, 227–236.
Billen, M., and M. Gurnis (2005), Constraints on subducting plate strength within the Kermadec trench, *J. Geophys. Res.*, *110*, B05407, doi:10.1029/2004JB003308.
Billen, M., and G. Hirth (2007), Rheologic controls on slab dynamics, *Geochem. Geophys. Geosyst.*, *8*, Q08012, doi:10.1029/2007GC001597.
Billen, M., and G. A. Houseman (2004), Lithospheric instability in obliquely convergent margins: San Gabriel Mountains, Southern California, *J. Geophys. Res.*, *109*, B01404, doi:10.1029/2003JB002605.
Buiter, S. J. H., M. J. R. Wortel, and R. Govers (1998), The role of subduction in the evolution of the Apennines foreland basin, *Tectonophysics*, *296*, 249–268.
Burov, E., and M. Diament (1992), Flexure of the continental lithosphere with multilayered rheology, *Geophys. J. Int.*, *109*, 449–468.
Byerlee, J. (1978), Friction of rocks, *Pure Appl. Geophys.*, *116*, 615–626.
Capitanio, F. A., and G. Morra (2012), The bending mechanics in a dynamic subduction system: Constraints from numerical modelling and global compilation analysis, *Tectonophysics*, *522-523*, 224–234.
Capitanio, F. A., G. Morra, and S. Goes (2007), Dynamic controls on subduction kinematics: The role of the downgoing lithosphere and passive mantle flow, *Earth Planet. Sci. Lett.*, *262*, 284–297.
Capitanio, F. A., G. Morra, and S. Goes (2009), Dynamics of plate bending at the trench and slab-plate coupling, *Geochem. Geophys. Geosyst.*, *10*, Q04002, doi:10.1029/2008GC002348.
Cizkova, H., J. van Hunen, and A. van den Berg (2007), Stress distribution within subducting slabs and their deformation in the transition zone, *Phys. Earth Planet. Inter.*, *161*, 202–214.
Conrad, C. P., and B. Hager (1999), Effects of plate bending and fault strength at subduction zones on plate dynamics, *J. Geophys. Res.*, *104*(B8), 17,551–17,571.
Craig, T. J., and A. Copley (2014), An explanation for the age independence of oceanic elastic thickness estimates from flexural profiles at subduction zones, and implications for continental rheology, *Earth Planet. Sci. Lett. 392*, 207–216.
Di Giuseppe, E., J. van Hunen, F. Funiciello, C. Faccenna, and D. Giardini (2008), Slab stiffness control of trench motion: Insights from numerical models, *Geochem. Geophys. Geosyst.*, *9*, Q02014, doi:10.1029/2007GC001776.
Eringen, A. C. (1967), *Mechanics of Continua*, John Wiley, N. Y.
Faccenda, M., L. Burlini, T. V. Gerya, and D. Mainprice (2008), Fault-induced seismic anisotropy by hydration in subducting oceanic plates, *Nature*, *455*, 1097–1100.
Faccenda, M., T. V. Gerya, and L. Burlini (2009), Deep slab hydration induced by bending-related variations in tectonic pressure, *Nat. Geosci.*, *2*, 790–793.
Faccenna, C., A. Heuret, F. Funiciello, S. Lallemand, and T. W. Becker (2007), Predicting trench and plate motion from the dynamics of a strong slab, *Earth Planet. Sci. Lett.*, *257*, 29–36.
Faccenna, C., E. Di Giuseppe, F. Funiciello, S. Lallemand, and J. van Hunen (2009), Control of seafloor ageing on the migration of the Izu Bonin Mariana trench, *Earth Planet. Sci. Lett.*, *288*, 386–398.
Funiciello, F., G. Morra, K. Regenauer-Lieb, and D. Giardini (2003), Dynamics of retreating slabs: 1. Insights from two-dimensional numerical experiments, *J. Geophys. Res.*, *108*(B4), 2206, doi:10.1029/2001JB000898.
Funiciello, F., C. Faccenna, A. Heuret, S. Lallemand, E. Di Giuseppe, and T. W. Becker (2008), Trench migration, net rotation and slab–mantle coupling, *Earth Planet. Sci. Lett.*, *271*, 233–240.
Gerya, T. V., and D. A. Yuen (2007), Robust characteristics method for modelling multiphase visco-elasto-plastic thermo-mechanical problems, *Phys. Earth Planet. Inter.*, *163*, 83–105.
Goetze, C., and D. Evans (1979), Stress and temperature in the bending lithosphere as constrained by experimental rock mechanics, *Geophys. J. R. Astron. Soc.*, *59*, 463–478.
Harder, H. (1991), Numerical simulation of thermal convection with Maxwellian viscoelasticity, *J. Non-Newtonian Fluid Mech.*, *39*, 67–88.
Heuret, A., F. Funiciello, C. Faccenna, and S. Lallemand (2007), Plate kinematics, slab shape and back-arc stress: A comparison between laboratory models and current subduction zones, *Earth Planet. Sci. Lett.*, *256*, 473–483.
Hoogenboom, T., and G. A. Houseman (2006), Rayleigh-Taylor instability as a mechanism for corona formation on Venus, *Icarus*, *180*, 292–307.
Karato, S., and P. Wu (1993), Rheology of the upper mantle—A synthesis, *Science*, *260*, 771–778.
Kaus, B. J. P., and T. W. Becker (2007), Effects of elasticity on the Rayleigh–Taylor instability: Implications for large-scale geodynamics, *Geophys. J. Int.*, *168*, 843–862.
Kohlstedt, D., B. Evans, and S. Mackwell (1995), Strength of the lithosphere: Constraints imposed by laboratory experiments, *J. Geophys. Res.*, *100*(B9), 17,578–17,602.
Leng, W., and S. Zhong (2010), Constraints on viscous dissipation of plate bending from compressible mantle convection, *Earth Planet. Sci. Lett.*, *297*, 154–164.
McAdoo, D. C., and D. T. Sandwell (1985), Folding of oceanic lithosphere, *J. Geophys. Res.*, *90*(B10), 8563–8569.
Moresi, L., F. Dufour, and H. B. Mühlhaus (2002), Mantle convection modeling with viscoelastic/brittle lithosphere: Numerical methodology and plate tectonic modeling, *Pure Appl. Geophys.*, *159*(10), 2335–2356.

Moresi, L., F. Dufour, and H. B. Mühlhaus (2003), A Lagrangian integration point finite element method for large deformation modeling of viscoelastic geomaterials, *J. Comput. Phys.*, *184*, 476–497.

Moresi, L., S. Quenette, V. Lemiale, C. Mériaux, B. Appelbe, and H.-B. Mühlhaus (2007), Computational approaches to studying non-linear dynamics of the crust and mantle, *Phys. Earth Planet. Inter.*, *163*, 69–82.

Morra, G., and K. Regenauer-Lieb (2006), A coupled solid-fluid method for modelling subduction, *Philos. Mag.*, *86*(21-22), 3307–3323.

Mühlhaus, H.-B., and K. Regenauer-Lieb (2005), Towards a self-consistent plate mantle model that includes elasticity: Simple benchmarks and application to basic modes of convection, *Geophys. J. Int.*, *163*(2), 788–800.

OzBench, M., et al. (2008), A model comparison study of large-scale mantle-lithosphere dynamics driven by subduction, *Phys. Earth Planet. Inter.*, *171*, 224–234.

Ranalli, G. (1995), *Rheology of the Earth*, 2nd ed., Chapman and Hall, London, U. K.

Ribe, N. M. (2010), Bending mechanics and mode selection in free subduction: A thin-sheet analysis, *Geophys. J. Int.*, *180*, 559–576.

Rose, I. R., and J. Korenaga (2011), Mantle rheology and the scaling of bending dissipation in plate tectonics, *J. Geophys. Res.*, *116*, B06404, doi:10.1029/2010JB008004.

Royden, L., and L. Husson (2006), Trench motion, slab geometry and viscous stresses in subduction systems, *Geophys. J. Int.*, *167*, 881–905.

Schellart, W. P. (2004), Quantifying the net slab pull force as a driving mechanism for plate tectonics, *Geophys. Res. Lett.*, *31*, L07611, doi: 10.1029/2004GL019528.

Stadler, G., M. Gurnis, C. Burstedde, L. C. Wilcox, L. Alisic, and O. Ghattas (2010), The dynamics of plate tectonics and mantle flow: From local to global scales, *Science*, *329*, 1033–1038.

Stegman, D., R. Farrington, F. Capitanio, and W. Schellart (2010), A regime diagram for subduction styles from 3-D numerical models of free subduction, *Tectonophysics*, *483*, 29–45.

Thielmann, M., and B. J. P. Kaus (2012), Shear heating induced lithospheric-scale localization: Does it result in subduction?, *Earth Planet. Sci. Lett.*, *359*, 1–13.

Turcotte, D., D. C. McAdoo, and J. Caldwell (1978), An elastic-perfectly plastic analysis of the bending of the lithosphere at a trench, *Tectonophysics*, *47*, 193–205.

Turcotte, D. L., and G. Schubert (1982), *Geodynamics*, John Wiley, N. Y.

Walcott, R. (1970), Flexural rigidity, thickness and viscosity of the lithosphere, *J. Geophys. Res.*, *75*(20), 3941–3954.

Watts, A. B., and S. Zhong (2000), Observations of flexure and the rheology of oceanic lithosphere, *Geophys. J. Int.*, *142*, 855–872.

Watts, A. B., J. H. Bodine, and M. S. Steckler (1980), Observation of flexure and the state of stress in the oceanic lithosphere, *J. Geophys. Res.*, *85*(B11), 6369–6376.

Wu, B., C. Conrad, A. Heuret, C. Lithgow-Bertelloni, and S. Lallemand (2008), Reconciling strong slab pull and weak plate bending: The plate motion constraint on the strength of mantle slabs, *Earth Planet. Sci. Lett.*, *272*, 412–421.

Yamato, P., P. Agard, E. Burov, L. Le Pourhiet, L. Jolivet, and C. Tiberi (2007), Burial and exhumation in a subduction wedge: Mutual constraints from thermomechanical modeling and natural P-T-t data (Schistes Lustres, western Alps), *J. Geophys. Res.*, *112*, B07410, doi: 10.1029/2006JB004441.